Investigating the excitonic properties of anisotropic bulk ReS_2 with photoluminescence spectroscopy

Nella Diepeveen
11785608

July 9, 2020

Study	Bachelor thesis Physics and Astronomy (15 EC) Conducted between 30-04-2020 and 09-07-2020
Supervisor	dr. J. van de Groep
Daily supervisor	M. van der Laan, MSc
Second examiner	prof. dr. P. Schall
Institute	Van der Waals-Zeeman Institute, Institute of Physics
Faculty	Faculteit der Natuurwetenschappen, Wiskunde en Informatica
University	Universiteit van Amsterdam

VU VRIJE UNIVERSITEIT AMSTERDAM

UNIVERSITEIT VAN AMSTERDAM

Populaire samenvatting

Duurzame energie wordt steeds belangrijker om klimaatverandering tegen te gaan. Zonne-energie opgewekt met fotovoltaïsche cellen (zonnecellen) is een goede oplossing hiervoor. Voor zonnecellen wordt halfgeleidermateriaal gebruikt. Als er licht op valt kunnen elektronen in het materiaal zich vrij bewegen en ontstaat er elektrische stroom. Een belangrijke ontwikkeling binnen zonnecellen zijn 2D halfgeleiders. Deze materialen bestaan uit individuele laagjes materiaal die opgestapeld zijn. Rhenium disulfide (ReS_2) valt onder deze groep 2D halfgeleiders en de mate waarmee het op licht reageert groeit met het aantal lagen, wat veel belovend is voor een nieuwe generatie zonnecellen. Een goede manier om halfgeleidermateriaal te bestuderen in door middel van fotoluminescentie. Bij fotoluminescentie absorbeert het materiaal licht en straalt daarna licht met een lagere energie uit. Als het een directe transitie betreft dan kan het licht meteen uitgezonden worden. Als het een indirecte transitie betreft dan is er een vibratie in het materiaal nodig voordat er licht kan worden uitgezonden. Hierdoor heeft het een minder goede interactie met licht. Daarom is het belangrijk om te weten of ReS_2 een directe of indirecte transitie heeft. In het materiaal kunnen elektronen en positieve "gaten" elkaar aantrekken met de Coulomb kracht, deze samengestelde deeltjes worden excitonen genoemd. Doordat de structuur van ReS_2 niet in alle richtingen hetzelfde is kunnen deeltjes in het materiaal zich anders oriënteren. In dit verslag voeren we fotoluminescentie metingen uit bij lage temperaturen om de eigenschappen van deze excitons nauwkeurig te bestuderen. We zien dat de kristal oriëntatie invloed heeft op het licht dat weer wordt uitgezonden.

Abstract

Rhenium disulphide (ReS_2) is a promising 2D semiconductor that belongs to the group VII transition-metal dichalcogenides. It has a strong light-matter interaction that grows with the number of layers, which makes it a promising candidate for thin-film solar cells. Its anisotropic crystal structure gives rises to unique fundamental properties. Using polarisation-resolved low-temperature photoluminescence measurement we investigate the influence of the crystal anisotropy on the photoluminescence. We observe two linear polarised excitons with an angle of $28(5)^\circ$ (X_1) and $115(5)^\circ$ (X_2) relative to the crystal b-axis. Temperature dependent measurements show a splitting of peaks in the photoluminescence spectrum when the temperature decreases. We study the (in)direct nature of the optical transition with excitation power dependent measurements. We observe that the X_1 exciton saturates faster than the X_2 exciton, which might be an indication of a lifetime difference or involvement of trions. Possible excited state of the two excitons are observed and for exciton X_1 fitted to a Rydberg series giving a binding energy of 144 meV. Combined, these results give important insights into the fundamental opto-electronic properties of ReS_2.

Contents

1 Introduction

With a rising concern about the environment and climate, there is a growing need for sustainable energy. Solar photovoltaics (PV) is set to grow the fastest of all renewable energy sources in 2020 [1]. Currently, most solar cells consist of bulk silicon or gallium arsenide [2]. A disadvantage of our current solar panels is that they take up a lot of space. This results in higher installation costs and they can only be installed on specifically designed sites. Solar cells made out of 2D materials would be a lot thinner and this would come with the advantage of flexibility and a reduction of material costs [3]. The use of 2D semiconductors enables partially transparent solar panels which opens up a whole new range of possible placements areas [4].

Transition-metal dichalcogenides (TMDs) are layered 2D materials with the formula MX_2, where M = transition metal and X = chalcogenide. The 2D crystal structure is built up out of a plane of metal atoms linked together with a metal-metal bond and that plane is sandwiched between two planes of chalcogenide atoms with covalent bonds. These monolayers are bonded together by weak van der Waals forces. The 2D monolayers exhibit no dangling bonds and due to the weak interaction between layers it is possible to exfoliate these to the monolayer limit. This gives a great opportunity to design heterostructures with other materials without concerns about lattice matching [5]. This means that 2D materials can be incorporated into already existing solar cells to enhance sunlight absorption by, for example, light trapping configurations [3]. Most TMDs have a direct bandgap as a monolayer and then transition to a indirect bandgap for multiple layers, resulting in a strong decrease in the light-matter interaction [6][7].

Rhenium disulphide (ReS_2) belongs to the group VII-TMDs but has some strikingly different properties than other TMDs. In contrast to most TMDs, ReS_2 seems to remain a direct bandgap with increasing layers which results in the light-matter interaction growing with the number of layers [5]. This gives an opportunity to make solar cells with thicker material instead of a monolayer as is needed for other TMDs in order to benefit from the direct bandgap. So far there has been a disagreement in the literature if there is an indirect bandgap in few-layer ReS_2. Density functional theory (DFT) calculations show that there is only a direct bandgap in a bilayer and for all other layers an indirect bandgap [8], while experimental measurements show a direct bandgap for all layers [9]. ReS_2 is also an anisotropic material which gives rise to unique physical properties [10]. It is unclear how the anisotropy has an effect on exciton formation, dynamics and their lifetime.

In this thesis we investigate the excitonic properties of bulk ReS_2 with polarisation-resolved photoluminescent spectroscopy to gain insight in the (in)direct nature of the optical transition. In particular, we study the influence of the crystal anisotropy and laser power on the photoluminescence at low temperatures.

1.1 Outline

The structure of this thesis is as follows. In chapter 2 we start with the description of the general properties of TMDs and ReS_2 and continue with background theory on bandgaps, excitons and photoluminescence. Next, in chapter 3, we explain the experimental setup and fabrication methods and continue with the general analysis that was done by spectral fitting. Then, in chapter 4, we discuss the results of the temperature and laser power dependence and polarisation-resolved photoluminescence and discuss the possible interpretations of the result.

Chapter 5 will discuss the results in the context of existing literature. Final conclusions and an outlook will be given in chapter 6.

2 Theory

2.1 Transition-metal dichalcogenides

Transition-metal dichalcogenides (TMDs) are materials with the formula MX_2, where M = transition-metal and X = chalcogenide. One layer is built up out of a plane of metal atoms linked together with a metal-metal bond and that plane is sandwiched between two planes of chalcogenide atoms with a covalent bond, shown in Fig. 1a. Each layer is bonded together by weak van der Waals bonds. The bulk version is built up out of these layers stacked on top of each other, and since each layer is free of dangling bonds, TMDs can be exfoliated to thin layers. Bulk TMDs are similar to a stack of paper, where you can remove one sheet by exfoliation in the same way that you can take a piece of paper from a stack of paper (mechanical exfoliation) [11]. This can be continued to the monolayer limit. Most TMDs transition from direct bandgap in monolayer to indirect bandgap in multiple layers because of a change in the band structure, due to quantum confinement, where the indirect transition becomes the lowest transition [6][7].

Rehnium disulphide (ReS_2) belongs to the group VII-TMDs. It has a distorted 1T-structure which reduces its hexagonal symmetry, seen in Fig. 1b. This gives rise to an in-plane anisotropy. The b-axis is parallel to the chain of Re-Re atoms. The unit cell contains four rhenium atoms and eight sulphur atoms and the angle between the a- and b-axis is 119.1° [12]. ReS_2 shows nearly layer-independent optoelectronic properties, which suggest a direct bandgap for all layers [5]. The photoluminescence will therefore increase with an increasing number of layers since there is a stronger light-matter interaction, until the incident light cannot penetrate further into the material due to the optical attenuation in the material according to the Beer-Lambert law [13]. Studies have observed that the photoluminescence increases with the number of layers until around eight layers from which it will remain constant [5]. Studies also showed a redshift of the photoluminescence with an increasing number of layers, which suggest a change in the size of the bandgap [9].

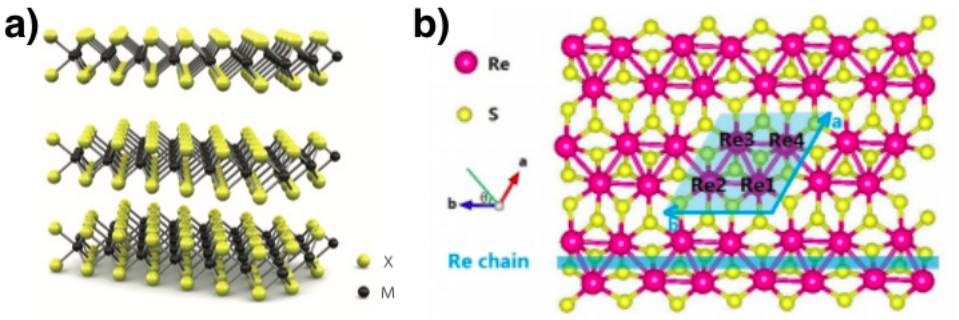

Figure 1: a) The general structure of a TMD. A plane of M atoms is sandwiched between two planes of X atoms. These are coupled with other layers with van der Waals bonds [14]. **b)** The crystal structure of ReS_2 with a distorted 1T-phase. The b-axis is parallel to the Re-Re chains. The unit cell is indicated by the blue box [12].

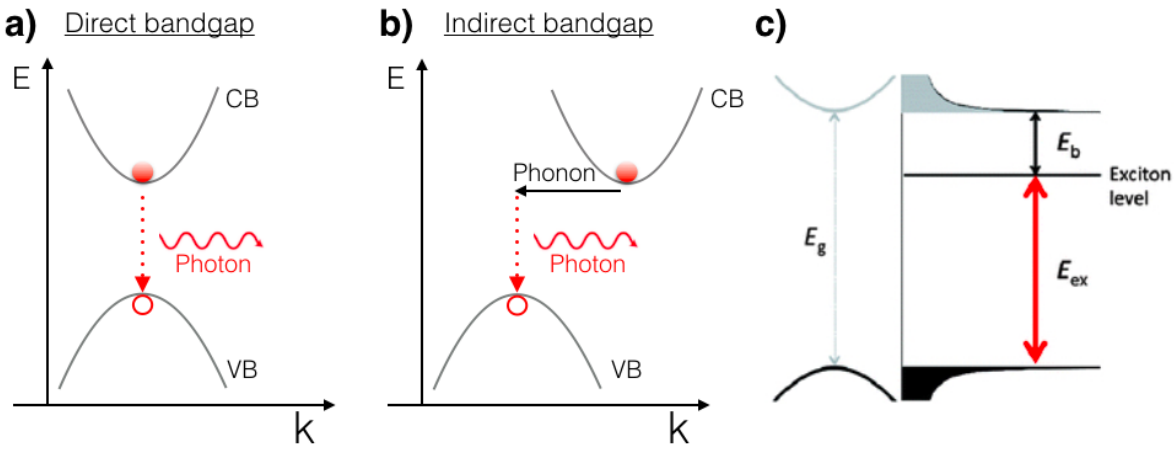

Figure 2: **a)** A representation of a direct bandgap. **b)** A representation of an indirect bandgap. **c)** Schematic energy level of an exciton where E_g is the bandgap, E_b is the exciton binding energy and E_{ex} is the optical energy of the exciton [15].

2.2 Bandgap

In a semiconductor the valence band (VB) and the conduction band (CB) are separated by an energy gap. The Fermi level lies in the middle of the bandgap for intrinsic semiconductors. This means that the states in the VB are completely filled, and the states in the CB are empty, except for thermal excitations. The bandgap for a semiconductor is small enough for an electron to get excited to the CB by the absorption of a photon [16]. An electron gets excited by a photon with an energy higher than the band gap. The electron leaves behind a positively charged hole. Both the electron and holes relax towards the minimum of the CB and the maximum of the VB, respectively. When the maximum of the VB is directly below the minimum of the CB in k-space, the bandgap is called direct. There is no extra momentum needed for the electron to fall back to the VB, as seen in Fig. 2a. A bandgap is indirect when the maximum of the VB is not directly above the CB in k-space. Thus, there is extra momentum needed for an electron to make the transition back to the VB, as seen in Fig. 2b. This extra momentum is provided by the interaction with a phonon which is a vibrational motion inside the lattice [16].

There are multiple processes that can affect the size of the bandgap, including temperature. An increase in temperature will increase the vibrations between the atoms in the lattice. This will increase the effective lattice spacing. Consequently, the periodic potential that the electrons experience will decrease and this will decrease the bandgap [17]. Hence, it is expected to see a redshift in the photoluminescence when the temperature is increased, which can be described by the empirically-determined Varshni equation:

$$E_g = E_0 - \frac{\alpha T^2}{\beta + T} \tag{1}$$

where E_g is the bandgap, E_0 is the bandgap at 0 K, and α, β are fitting parameters [18]. The β-parameter has often been found to be in close relation with the Debye temperature of the material, which is the temperature at which the highest-energy phonon mode is excited [19][20].

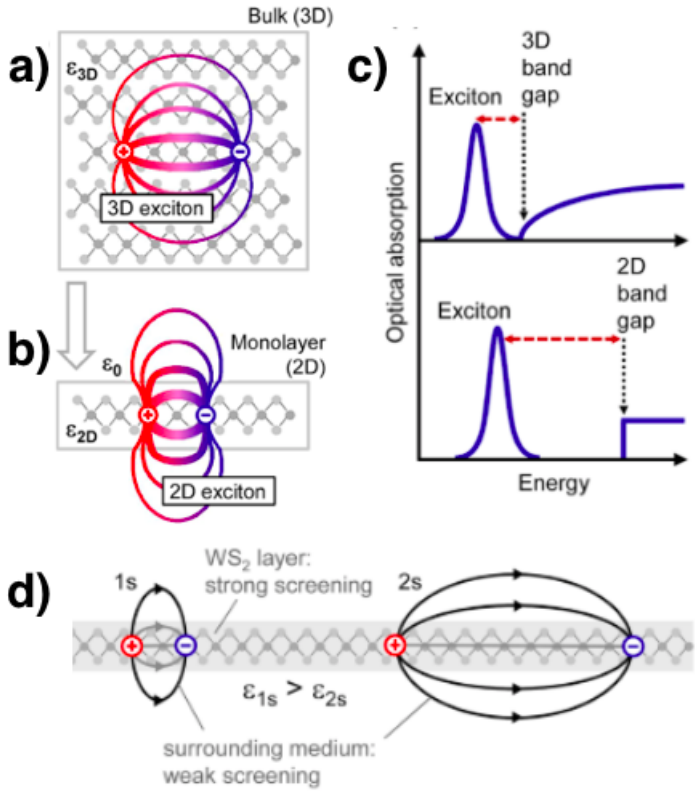

Figure 3: **a)** Exciton representation in a 3D crystal lattice. **b)** Exciton representation in a 2D monolayer where the monolayer has a different dielectric constant than the surrounding environment. **c)** The change in bandgap and excitonic binding energy due to a reduction in dimensionality. **d)** Representation of an excited state of an exciton [21].

2.3 Excitons

When an electron is excited to the CB by a photon it leaves behind a positively charged hole, where the electron was. Since the electron and hole have opposite charge, they are attracted to each other via the Coulomb force, like the hydrogen atom. The electron and hole can form a bound (quasi-particle) state, resulting in a slightly lower energy than the free hole and electron, as seen in Fig. 2c. Where E_g is the band gap energy, E_b is the exciton binding energy and E_{ex} is the energy that is released by for example a photon when the electron combines with the hole. Since the electron and hole are attracted to each other, there is energy needed to break this apart into a free hole and electron, which is called the binding energy.

The energy of excitons in TMDs depends on the number of layers of the material. There are two processes that have an effect on the energy, namely reduced screening of the Coulomb interaction and quantum confinement. In a 3D material, electric field lines between the electron and hole are screened by the positive atoms and negative electrons between them, as seen in Fig. 3a. The positive atoms and negative electrons will give a polarisation opposite to the electric field lines of the electron and hole. This has as an effect that the electron and hole feel each other less, thus lowering their binding energy. In a 2D material the exciton is

confined to the 2D plane. As such, the electric field lines of the exciton extend outside the plane where the dielectric constant is lower, thereby reducing the screening, as seen in Fig. 3b. Additionally, in a 2D plane the electrons and holes are closer together, as seen when comparing Fig. 3a and 3b, which increases there Coulomb attraction. Both the reduction of screening and the increased Coulomb interaction results in an increase in E_b of the exciton.

The other effect is quantum confinement. When the number of layers is decreased the allowed electron wavefunction becomes shorter and the bandgap increases [21]. In 3D the density of states is proportional to the square root of the energy ($DoS \propto \sqrt{E}$). When lowering the dimensionality from 3D to 2D the width of the material becomes comparable to the effective de Broglie wavelength of the carriers. Consequently, the motion of the carriers is restricted to a 2D plane and are therefore placed in a potential well. Therefore, for 2D materials the density of states changes to a step function with discrete values [22]. This is seen in Fig. 3c. If the bandgap E_g grows more than the exciton binding energy E_b, the exciton energy E_{ex} becomes bigger [21]. The typical exciton E_b in TMDs is 300-500 meV in monolayer and 10-150 meV in bulk [23][24]. When the binding energy is bigger than the thermal energy ($E_b > k_bT$) stable excitons can be formed. In normal semiconductors the binding energy is smaller than the thermal energy and the excitons becomes free holes and electron. However, for TMDs the large binding energy result in stable excitons even at room temperature ($k_bT = 25$ meV). This is the reason why excitonic effect are important in TMDs, and dominate the optical response.

It's also possible to have excited exciton states, similar to that of the hydrogen atom. The ground state is a 1s-orbital. The excited state are 2s, 3s orbitals, etc. A physical representation is seen in Fig. 3d. In an excited state the hole and electron are further apart thus the Coulomb attraction is lower since it scales as $1/r^3$, thus the binding energy scales with the quantum number and is smaller. However, more electric field lines between the electron and hole are extended outside the material to a medium with a smaller dielectric constant. Consequently, there is less screening which makes the binding energy higher. The effect of the reduced Coulomb interaction is larger than the reduced screening, thus the excited state will have a lower binding energy and a higher optical energy [21]. To observe excited states the temperature needs to be low enough, so the binding energy is higher than the thermal energy ($E_b > k_bT$). Since the binding energy of the excited states is lower than the groundstate, the excited states are typically only observed at lower temperatures. An exciton with excited states in 3D can be described by the 3D Wannier excitons in inorganic semiconductors formula given by,

$$E_b^{(n)} = E_g - \frac{Ry^*}{n^2} \tag{2}$$

where E_g is the bandgap, n is the quantum number of the exciton state, $E_b^{(n)}$ is the binding energy at nth excitonic state and Ry^* is the effective Rydberg constant [9][25]. For exciton with excited states in a 2D material the change in dielectric environment needs to be taken into account [21].

Finally, a trion is an exciton bound to another electron or another hole. It can thus be positively or negatively charged. Since the binding energy is defined as the energy needed to remove the excessive charge, then in the case of a trion it leaves behind an exciton. It is therefore expected to have a larger binding energy than an exciton and E_{ex} is smaller.

2.4 Photoluminescence

In a semiconductor, electrons in the VB can get excited to the CB by absorbing a photon with an energy larger than the bandgap. The electron and hole then undergo momentum and energy relaxation to the minimum of the CB and the maximum of the VB respectively, and can form an exciton as described above. This relaxation can be due to interaction with phonons [25]. The process where the electron then decays radiatively to the VB is called photoluminescence (PL). In a PL measurement it is expected to see the strongest emission from the lowest possible transition between the CB and VB.

By pumping a lot of electron towards the CB the PL is expected to increase since there will also be more recombination events. However, there comes a point when there are no electrons left at the top of the VB. Thus, there will be no excitations until an electron decays and recombines with a hole. Then this electron can be excited again. This means there is saturation of the PL intensity. How quickly this effect happens depends of the lifetime of the exciton. If it has a very short lifetime it will decay quickly and can thus be excited again. If the lifetime is longer it will take longer to decay and the re-excitation will also take longer, which means the saturation of the PL will happen quicker [26] [27].

When the number of excitons increases, the excitons can annihilate each other via the Auger process (bi-exciton annihilation) [28]. Two excitons come across each other and one of the excitons can give its energy to the other, leaving just one exciton in a higher energy state. This exciton can non-radiatively decay towards its original energy state and then radiatively decay towards the VB. This leaves one photon emitted for originally two excitons in total thus saturating the PL. This also depends on the lifetime of the excitons. Because the longer the lifetime, the bigger the probability of two excitons finding each other to annihilate [29].

3 Methods

3.1 Sample Fabrication

The sample is fabricated by exfoliating ReS_2 (purchased from HQ-Graphene) on an Ossila standard sapphire substrate using Nitto SPV-224PR-MJ blue tape. ReS_2 is exfoliated around 5 times, by touching the sticky sides of the tape together, before placing the ReS_2 flake on the sapphire substrate. To clean the sample we submerge it in isopropanol for 5 minutes and thereafter in ethanol for 5 minutes. Before measurements on the flake at low temperatures the exfoliated sample is baked at 120°C for approximately 40 minutes to outgas any surface adhesion. An exfoliated flake is seen in Fig. 4a. There is a clear breaking line between two different layer thicknesses which are both expected to be bulk based on their PL spectrum. Fig. 4b shows the crystal structure of ReS_2 from a top view, where the purple dots are rhenium atoms and green dots are sulphur atoms. The b-axis is parallel to the chain of rhenium atoms. Because of the strong metal-metal bonds between the rhenium atoms we expect the ReS_2 to break along the b-axis [30]. A sharp breaking line between two different layers, as seen on the flake in Fig. 4a, is thus expected to be the b-axis. A raman spectrum of this ReS_2 flake with the sapphire substrate at a temperature of T = -195.8°C is seen in Fig. 4c. The blue spectrum is for ReS_2 on sapphire and the red spectrum is for bare sapphire. The biggest raman peaks for both materials are indicated and correspond to the literature values [5][31][32], confirming that the flake is ReS_2. The inset in Fig. 4c shows the atomic displacements for the in-plane vibrations of Re atoms (E_g).

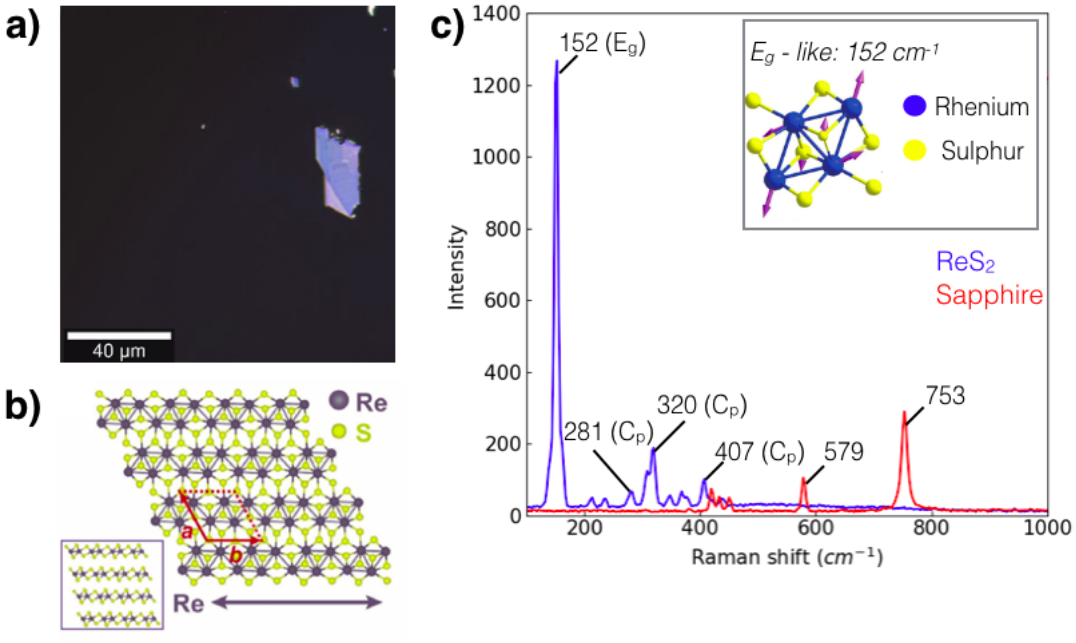

Figure 4: **a)** Optical microscope image of an exfoliated flake on a sapphire substrate. **b)** Crystal structure of ReS_2 [33]. The b-axis is parallel to the rhenium atoms. **c)** Raman spectrum of ReS_2 (blue) and sapphire (red), with energies of the biggest raman peaks indicated. The inset show the atomic displacements for the in-plane phonon mode E_g (152 cm^{-1}) [34].

3.2 Setup

A schematic of the experimental setup is shown in Fig. 5. We use a Witec 300 alpha R confocal microscope indicated by the dashed line. For reflection measurements we use a halogen lamp where the light is collimated by a collimating lens. For PL and raman measurements we use a diode-pumped solid-state laser with a wavelength of $\lambda = 532$ nm. The power of the laser can be tuned with the laser pinhole, to a maximum of 75 mW. The laser light is coupled into a single mode polarisation-maintaining fiber. The laser then gets coupled into the microscope system and passes a collimating lens and a $\lambda/2$-waveplate which rotates the polarisation of the laser light. By default, it is linear polarised with angle of 0° with respect to the horizontal axis seen in Fig. 4a and can be adjusted over 360° with a movable wheel. The laser passes a 532 nm long pass Raman filter and laser line filter stacked op top of each other which reflects the laser light downwards towards the sample, and filters the reflected laser light so it does not reach the detector.

The sample is either on a piezo stage or in a cryostat (Linkam THMS350EV stage) with a vacuum and cooling system (FDCS196 Freeze drying system). The piezo stage is moveable and can make a piezo scan of a part of the sample. In the cryostat the sample lies on a silver stage that is cooled by liquid nitrogen and has a temperature range from -195°C to 350°C. To provide good thermal conductance a small droplet of immersion oil of 2 μL is placed between the silver stage and the sample. The air in the cryostat chamber gets pumped at by a vacuum pump resulting in a typical pressure at low temperatures of $1.5{\cdot}10^{-3}$ mbar. The power of the laser is measured with a power meter (Thorlabs PM100USB with a "S120C" silicon sensor) which can be placed manually between the objective and the cryostat/piezo stage.

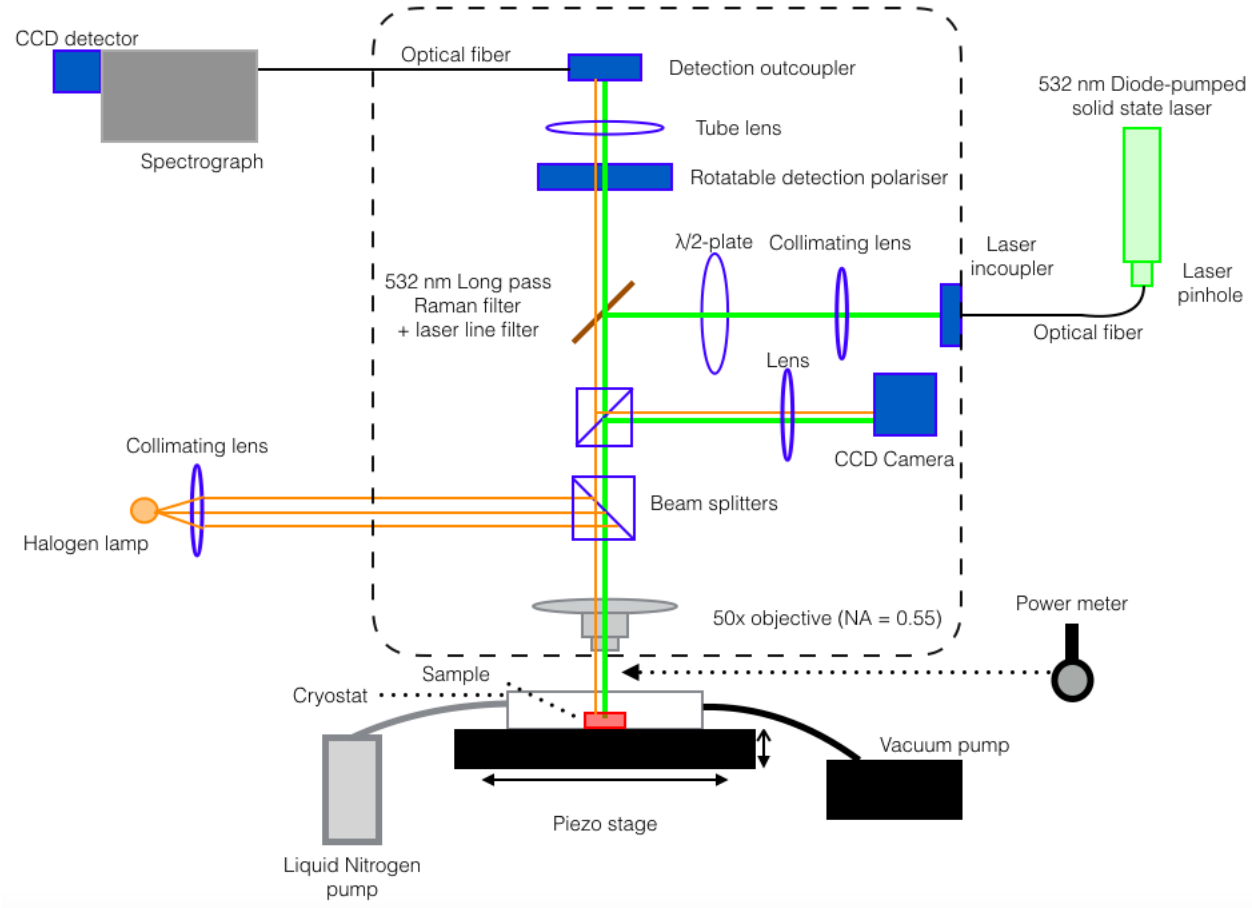

Figure 5: Schematic view of PL, raman, and reflection setup

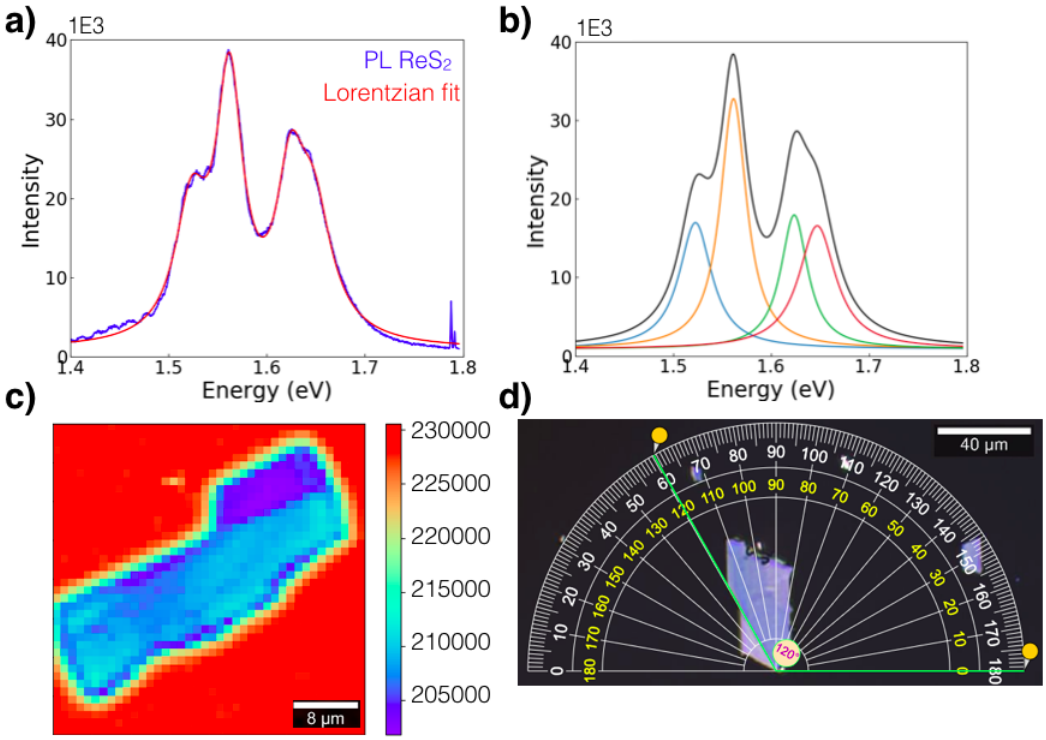

Figure 6: **a)** A typical PL spectrum at low temperature (blue) with a fit consisting of the sum of 4 lorentzian functions (red). The peaks at 1.80 eV are raman peaks. **b)** Lorentzian fit split up into its 4 separate peaks. **c)** A piezo scan of a ReS_2 flake where each point represents a sum of the PL spectrum between 1.35 eV and 1.7 eV. The sapphire substrate (red) has a higher PL than ReS_2. There are two different layer thicknesses observed as purple and blue. **d)** Calculation of the angle of the b-axis with the horizontal axis giving an angle of 120°.

The signal from the sample is collected by a 50x objective with numerical aperture NA=0.55 (Zeiss 50x LD Epiplan-Neofluar, NA=0.55, working distance (WD) = 9.1 mm). The beam splitter can be set to brightfield, where we look at reflection and scattering or on darkfield, where we only look at scattering. For raman and PL measurements the darkfield setting is used. For reflection measurements the brightfield setting is used. The signal then passes another beam splitter which directs the light either towards the CCD camera or the detector. Towards the detector, the signal passes a rotatable detection polariser which filters out a specific polarisation from the signal. It ranges between +90° and -90° with steps of 5°. For our polarisation-dependent measurements steps of 15° are used. The signal from the sample passes a tube lens and then gets coupled into a spectrograph (Witec UHTS 300 Vis) which has three gratings all blazed for 500 nm: 150, 300 and 600 gr/mm. For raman measurements we use the 600 gr/mm which gives the highest resolution but has a narrow spectral range. For PL we use the 150 or 300 gr/mm for a wider spectral range. Attached to it is a CCD detector (Andor EMCCD) which operates at -60°C.

3.3 Measurements and Analysis

All PL spectra are taken with an integration time of 10 seconds and 5 accumulation and a dark spectrum is subtracted. We fit the PL spectra with a sum of lorentzian functions given by

$$L(x) = \frac{1}{2\pi} \frac{\Gamma}{(x - x_0)^2 + (\frac{1}{2}\Gamma)^2} + c \tag{3}$$

where Γ is the Full Width at Half Maximum (FWHM), x_0 is the central position and c is the offset [35]. A typical PL spectrum with a four-lorentzian fit is shown in Fig. 6a, where the PL spectrum is in blue and the fit with 4 lorentzians in red. To calculate the total contribution of each peak to the spectrum we split up the total fit into the separate peaks, as shown in Fig. 6b, and then integrate each peak over twice its FWHM. To calculate the error of the integral we use the error of the total fit with the propagation of error analysis and then use this error in the range of twice the FWHM of each peak [36]. A piezo scan of a ReS_2 flake is shown in Fig. 6c. The laser power is 5.83 mW and each point represents a sum of the PL spectrum between 1.35 eV and 1.7 eV. There are 2 clear layer thicknesses visible for the flake (purple and blue layer). The PL from the sapphire substrate is higher than from ReS_2 as seen in red, due to defect states. However, the PL from the sapphire substrate is reduced by the bulk ReS_2 flake.
To see how the laser power affects the PL spectra we measure the PL spectra at different laser powers approximately between 0.5 to 20 mW. Assuming that the laser is a Gaussian beam, the intensity of the laser spot is related to the power by

$$I_{laser} = \frac{\pi \mathrm{NA}^2 P}{\lambda_0^2} \tag{4}$$

where NA is the numerical aperture of the objective, P is the laser power and λ_0 is wavelength of the laser [37]. We then integrate the PL of each peak at different powers and fit it to a power function given by

$$I_{PL} = \alpha P^{\beta} \tag{5}$$

where α and β are both constant.

To observe how the crystal anisotropy has an effect on the PL spectra we measure polarisation-resolved PL in a range between of +90° and -90° with steps of 15°. These polarisation angles are of the electric field with the horizontal axis in the setup. This can be transformed into a polarisation of the electric field with respect to the b-axis of ReS_2 by calculating the angle of the b-axis with the horizontal axis as seen in Fig. 6d with the use of a online tool [38]. The exciton orientation is determined by fitting the integrated PL as a function of polarisation angle to the function

$$I(\theta) = I_0 + I_1 \cos^2(\theta - \theta_{max}) \tag{6}$$

where I_0 and I_1 are the minimal and maximal integrated PL respectively and θ_{max} is the polarisation angle at which the integrated PL is maximized [30].

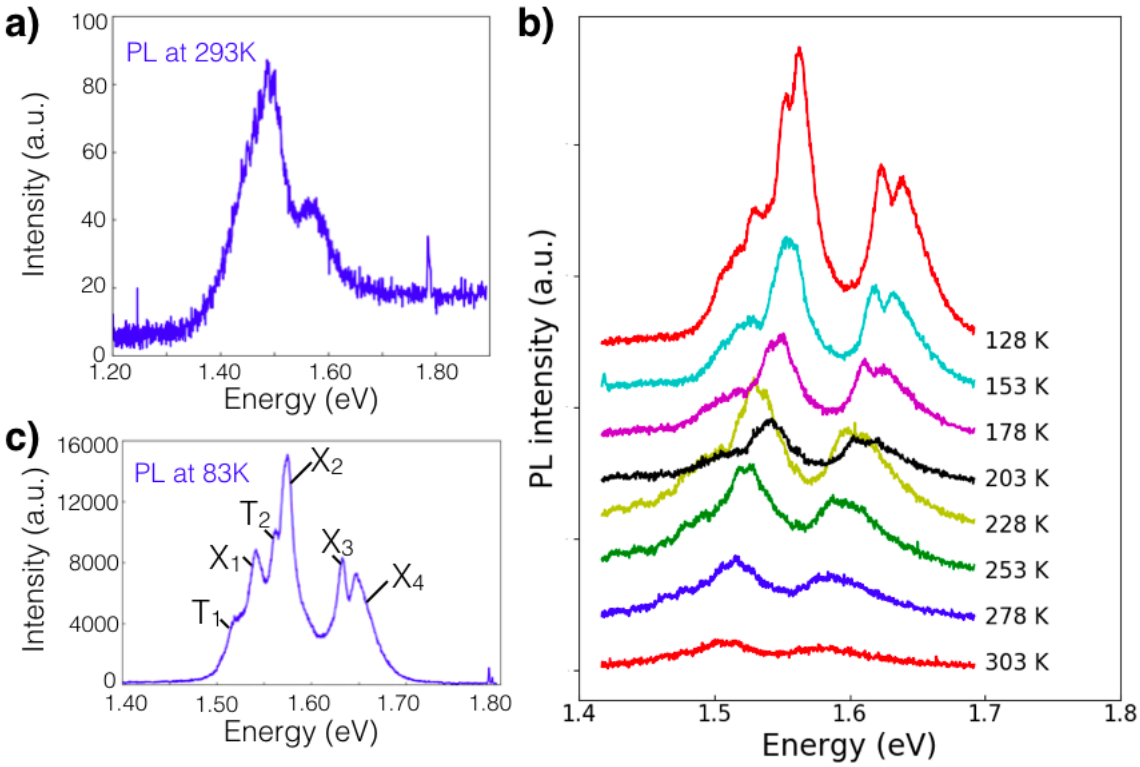

Figure 7: **a)** PL spectrum of ReS_2 at room temperature. There are two peaks visible. The little peaks at 1.8 eV are raman peak of the sapphire substrate. **b)** PL spectrum at decreasing temperature with steps of 25 K. The left peak grows into four peaks as the temperature decreases and the right peak into two. The black spectrum at 203 K does not follow the trend due to water condensation on the flake. **c)** PL spectrum at 83 K with all peaks labelled.

4 Results

4.1 Temperature dependence

First, we study the PL spectrum at room temperature to obtain a primary view on the characteristic PL peaks. A PL spectrum at a pump laser power of 1.80 mW is shown in Fig. 7a. The small peaks at 1.8 eV are raman peaks of the sapphire substrate. Also, the spectrum does not go down to zero at higher energies because of the raman signal which occurs around 2.0 eV. There are two peaks visible at 1.5 eV and 1.58 eV, but it is unclear where they come from. Due to the high temperature there is a lot of phonon scattering resulting in broadened peaks. The average phonon number is given by the Planck distribution and depends on temperature and the energy of the phonon [20]:

$$\langle n \rangle = \frac{1}{e^{\frac{E_{ph}}{k_B T}} - 1} \tag{7}$$

The number of phonons reduces as the temperature decreases, resulting in a less phonon scattering thus sharper PL peaks. Thus, to get a clearer view of the peaks we need to look at lower sample temperatures. Fig. 7b shows PL spectra at a temperature between 303 K

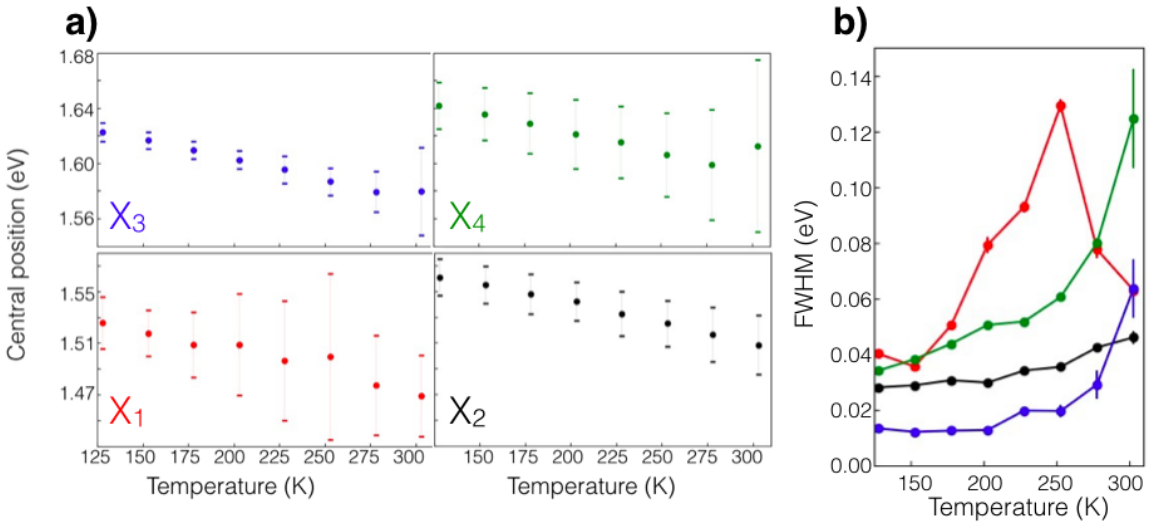

Figure 8: a) The central position of the exciton peaks as a function of temperature with the FWHM as error. There is a clear blueshift for exciton peaks X_2 and X_3 as the temperature decreases. For exciton peaks X_1 and X_4 a blueshift is less visible due to a large FWHM. **b)** The FWHM as a function of temperature. There is a clear decrease in FWHM as the temperature decreases. The FWHM of X_1 is lower for the highest temperature due to the fact that the fit was not good since the peak was not clearly visible.

and 128 K with steps of 15 K. As the temperature decreases, the peaks become narrower and more peaks become visible. The black spectrum at 203 K does not follow the trend, this is likely due to water condensation on the flake. When the temperature decreases, the left peak at 1.5 eV splits up into 4 peaks and the right peak splits up into 2 peaks. This already shows that rich excitonic behaviour governs the PL.

Fig. 7c shows the PL at 83 K with a pump power of 1.245 mW. There are 6 peaks visible indicated with names for future reference. The dependence on temperature of the central position of the peaks X_1, X_2, X_3 and X_4 is shown in Fig. 8a, with colours red, black, blue and green respectively. There is a clear blueshift for exciton peaks X_2 and X_3 as the temperature decreases as expected from theory section 2.2. The positions of X_1 and X_4 shows a bit of fluctuation and a large error, probably due to the fact that the peaks only become well pronounced at 178 K. The FWHM of the peaks as a function of temperature is shown in Fig. 8b. For all peaks there is a clear decrease in FWHM as the temperature decreases which is also as expected since there is less phonon scattering at lower temperatures. The FWHM of X_1 is lower for the highest temperatures due to the fact that the fit was not good since the peak was not clearly visible. The peak position at a temperature of 83 K and a pump power of 1.245 mW are 1.54(4) eV, 1.570(20) eV, 1.63(3) eV and 1.65(3) eV for X_1, X_2, X_3 and X_4 respectively.

For now we will focus on the two large left peaks, exciton X_1 and exciton X_2, because these two peaks are observed the most in literature [9][30][39]. The first thing to notice in Fig. 7c is that the PL intensity of exciton X_2 is higher than exciton X_1. This is not expected since PL normally shows the lowest energy transition as the highest peak. The difference in peak intensity therefore gives an indication that exciton X_2 decays faster than exciton X_1 and thus suggests a shorter lifetime [30]. Which means that exciton X_2 might tend to scatter

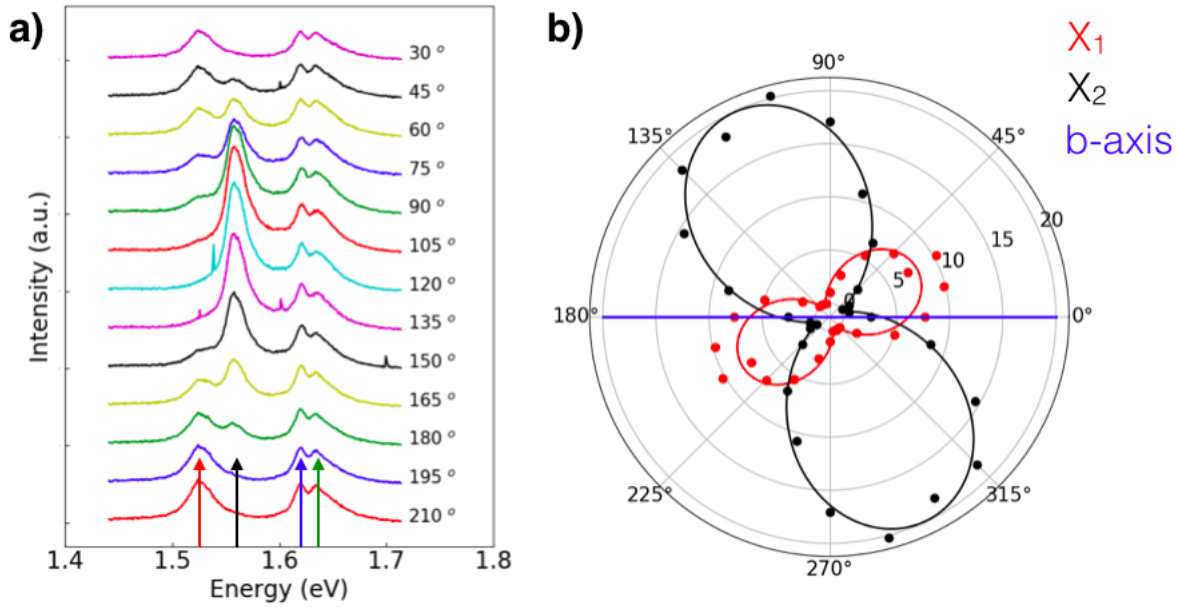

Figure 9: **a)** PL spectra detected at different polarisations with respect to the b-axis in steps of 15°. Four peaks are indicated by arrows. There is a clear dependence on polarisation for the red and black peaks. **b)** A polar plot of the excitons X_1 (red) and X_2 (black). The radius is given by the integrated PL of the peak and set out against the polarisation with the b-axis (blue line). Both show a double-lobed structure which is fitted with $I(\theta) = I_0 + I_1 \cos^2(\theta - \theta_{max})$ giving a maximum angle of $\theta^1_{max} = 28(5)°$ for X_1 and $\theta^2_{max} = 115(5)°$ for X_2.

towards the energy of exciton X_1 but it needs to overcome a barrier and before it can do that it already decays. This barrier might be due to a different orientation in the crystal structure due to the anisotropy.

4.2 Polarisation-resolved PL

To get a clearer view on the difference between the two exciton peaks we look at polarisation-resolved PL. The b-axis of the flake is 120(5)° compared to the horizontal axis as shown in Fig. 6d. PL spectra at different polarisations respective to the b-axis are shown in Fig. 9a. It shows the PL between 30° and 210° with steps of 15°. The positions of exciton X_1 and exciton X_2 are indicated with a red and black arrow, respectively. There is a clear dependence of the peak height on the polarisation angle. Exciton X_1 seems to be at its maximum at 210° and then drops in amplitude until it reaches a minimum at 120°, while exciton X_2 seems to do the opposite. To quantify the polarisation dependence we take the integral of each peak and plot this in a polar plot. The points are plotted at the polarisation angle and with a radius equal to the integral and then fitted to equation 6.

The result is seen in Fig. 9b. Exciton X_1 and exciton X_2 are plotted red and black respectively and the b-axis is at an angle of 0° as indicated by the blue line. They both show a double-lobe structure but with a maximum at different polarisations. The maximum polarisation angle for exciton X_1 and exciton X_2 are $\theta^1_{max} = 28(5)°$ and $\theta^2_{max} = 115(5)°$,

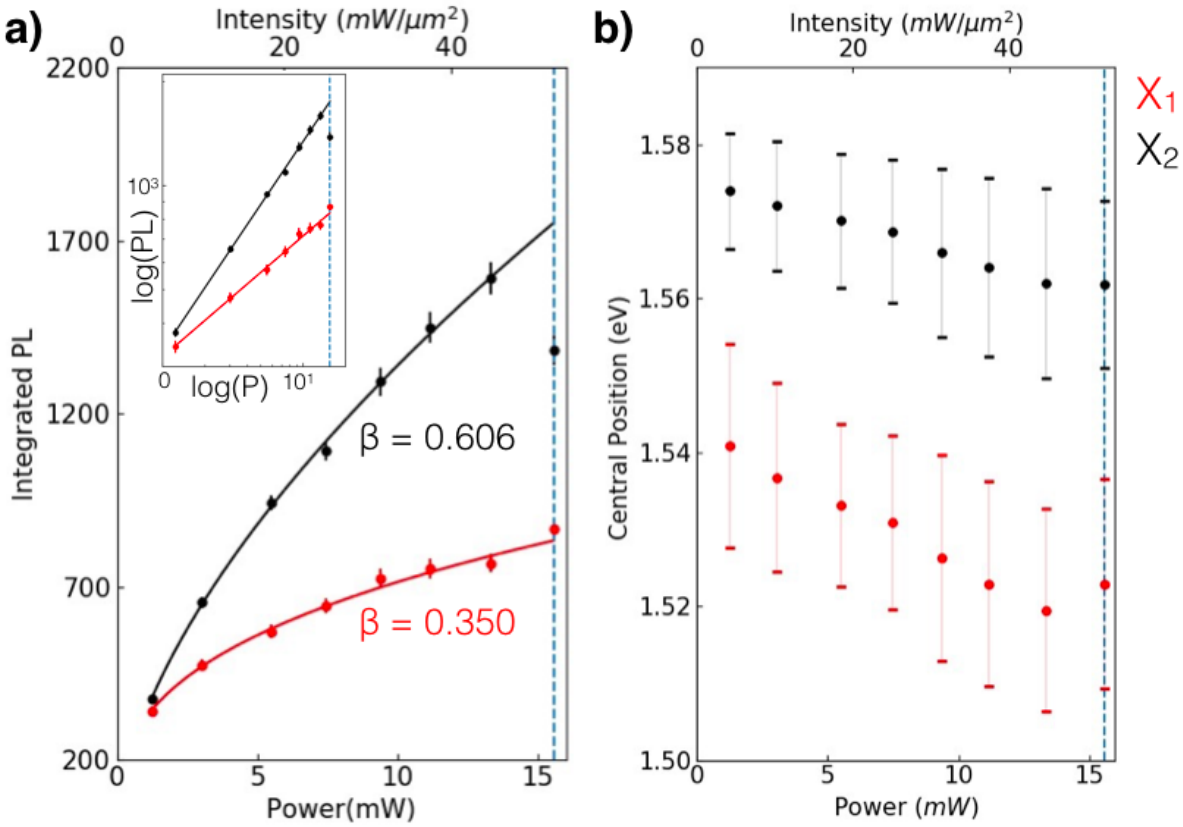

Figure 10: a) The integrated PL for exciton 1 (red) and exciton 2 (black) as a function of laser power. The dashed blue line indicates when the sample got burned. Both dataset are fitted with the power function $I_{PL} = \alpha P^{\beta}$ and the β-parameter is shown for both excitons. The inset shows a log-log plot where the β-parameter is the slope. **b)** The central position of exciton 1 (red) and exciton 2 (black) as function of power with the FWHM as error. It shows a redshift for both excitons for higher power.

respectively. These values correspond to the literature values found for bulk [30][39]. This thus shows a clear dependence on the exciton orientation due to the anisotropy in the material. It might also be a possible reason why it is difficult for exciton X_2 to scatter towards the energy of exciton X_1 since the excitons are oriented differently in the crystal structure.

The laser polarisation also needs to be taken into account. In the measurements the laser is polarised at 0°, which means that it has an angle with 120° with the b-axis. This is very close to the maximum of exciton X_2. To check if this does or does not give a priority towards X_2, measurements at different laser polarisations need to performed. Thus, the exciton peaks at 1.54 eV and 1.57 eV clearly correspond to excitons with different orientations, due to the crystal anisotropy.

4.3 Saturation

To get another insight into the difference between exciton X_1 and exciton X_2 and study the directness of the transition, we look at the power dependence of the exciton PL. The

integrated PL as a function of power is shown in Fig. 10a. On the top horizontal axis the intensity in $mW/\mu m^2$ calculated with equation 4 is shown. Exciton X_1 is shown in red and exciton X_2 is shown in black. The dashed blue line indicates the damage threshold at which the sample was burned (P = 15.57 mW). Data points beyond this line are not trustworthy. The data points are fitted with the power function given by equation 5 and the β-parameter is shown for each fit. The inset of Fig. 10a shows a log-log plot where β is the slope and α is the offset. The error for the integrated PL grows when going to higher power. A reason for this is that the peaks get broader at higher laser powers. In consequence, the fit does not work as well for larger powers thus creating a larger error.

For the power function fit the parameters for exciton X_1 are: $\alpha = 318(7)$ and $\beta = 0.350(11)$. For exciton X_2 they are: $\alpha = 331(5)$ and $\beta = 0.606(8)$. Exciton X_1 saturates faster than exciton X_2, which suggest that exciton X_1 has a longer lifetime and thus decays slower than exciton X_2 if we assume that the saturation is dominated by the process described in section 2.4. The result is not conclusive to say anything about the direct or indirect nature of the transitions, only that there is a possible difference in lifetime. However, both exciton peaks have an intensity of the same order of magnitude. This indicates that the exciton peaks are either both direct or both indirect.

The central position of the two excitons as a function of power is shown in Fig. 10b. Both peaks show a redshift as the power increases. However, due to large error this cannot be said for certain. Measurements at lower temperature need to be done to decrease the FWHM and thus the error to show conclusive results. A redshift at higher laser power could be due to bandgap renormalisation [23]. When there is a high laser power, a lot of electron are excited to the CB resulting in more free charge carriers. This will increase screening resulting in a lowering of the binding energy of the excitons which would result in a blueshift. At the same time there is a reduction of repulsive Coulomb interaction between charges of the same sign. This will decrease the quasi-particle energy and lead to a bandgap renomalisation where the size of the bandgap decreases. In total there will be a redshift in central position of excitons, in agreement with our observations.

Another explanation for the redshift of the two excitons is the presence of trions. Going back to Fig. 7c we see on the left side of both the excitons two little bumps, labelled T_1 and T_2, which we attribute to trions. The difference between the position T_1 and X_1 is 22.85(26) meV at a power of 1.245 mW and for T_2 and X_2 it is 14.16(14) meV. This is comparable to literature values of trion binding energies, and trion peaks are commonly observed at low temperatures [40][41][42].

Studies have shown that in monolayer TMDs, too high generation rates are not advantageous for excitons [43]. When the laser power is increased, more electrons holes are generated thereby also generating more excitons. This could lead to more exciton-exciton annihilation, thus saturating the contribution of the excitons in the PL spectra. The trion density in determined by the background free-carrier density. By increasing the generation rate the trion recombination rate is also expected to increase but models have shown that the trions are not affected as much by annihilation [43]. This could thus result in a higher trion contribution in the PL spectra than the exciton contribution. Fig. 11 shows the PL spectra at the measured laser powers. As the laser power increases the contribution of both T_1 and T_2 seems to grow more than of X_1 and X_2. This gives a hint towards the hypothesis that trions become more important than excitons at higher power.

Thus, the saturation might be due to the fact that exciton-exciton annihilation becomes an important factor in the exciton recombination rate. While the redshift might come from

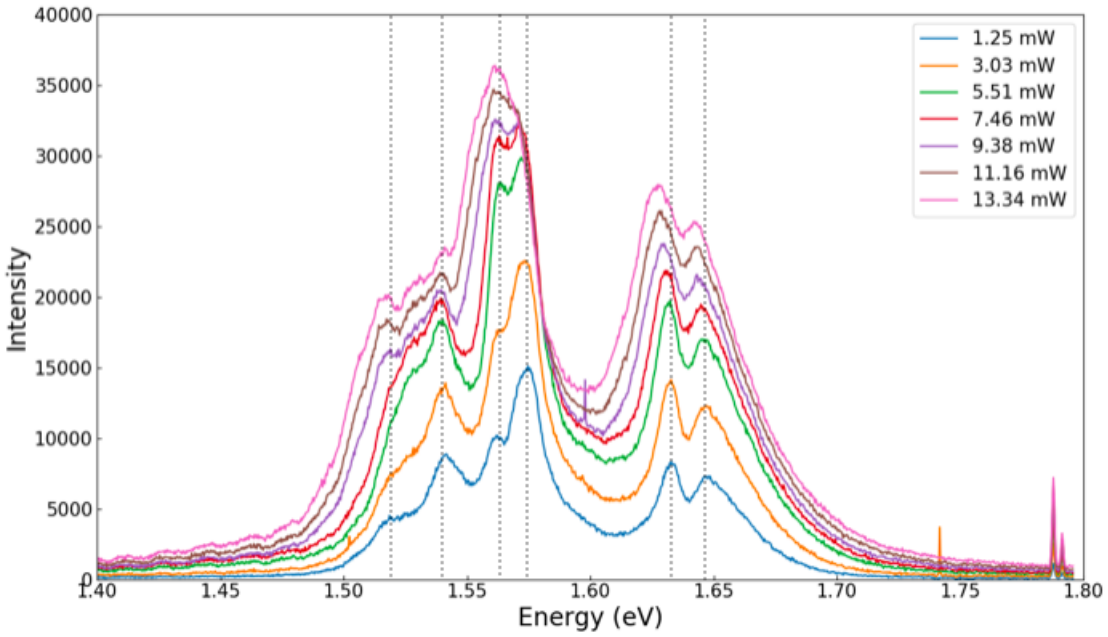

Figure 11: PL spectra at increasing laser power. The peaks of T_1 and T_2 grow more than X_1 and X_2. There is a small spectral shift for the X_3 and X_4 peaks.

the increasing presence of the radiative trion recombination in PL. To say more about the saturation, we need to do lifetime measurements to see if there is an actual difference between the lifetimes of excitons X_1 and X_2. To know more about the possibility of trions we need to for example change the charge density in the material by doping or applying a backgate voltage.

4.4 Possible excited states

Going back to Fig. 7c, we see two additional peaks at higher energies labelled X_3 and X_4. Comparing them to literature suggest that they could possibly be attributed to excited states of X_1 and X_2 [9]. It is expected that the excited states have the same polarisation dependence as their groundstate due to the similar orbital nature (1s, 2s). The polarisation-resolved PL measurement does not show clear data to confirm this.

However, reflection measurements done on the same flake as the saturation measurements with the same setup do show a clear polarisation dependence as shown in Fig. 12 [44]. Fig. 12a shows the polarisation dependence of excitons X_1 and X_2 from reflection measurements. Both excitons have the same shape as seen in Fig. 9b, which demonstrates the impact of the crystal anisotropy on the exciton orientation. The maximum polarisation angle for X_1 and X_2 is 14(5)° and 92(5)° with respect to the b-axis. This measurement was done on another flake than the polarisation-resolved PL measurements but still bulk. The biggest error between the two is the measured value for b-axis which is around 5°. The polarisation dependence of the possible excited states is shown in Fig. 12b. Exciton X_3 and X_4 in blue and green respectively. They both show a clover-like shape with maxima at the same angles as exciton X_1 and X_2. This indicates that the both peaks are a superposition of excited states of both polarisations. To know this for certain, lower temperature measurements are required which

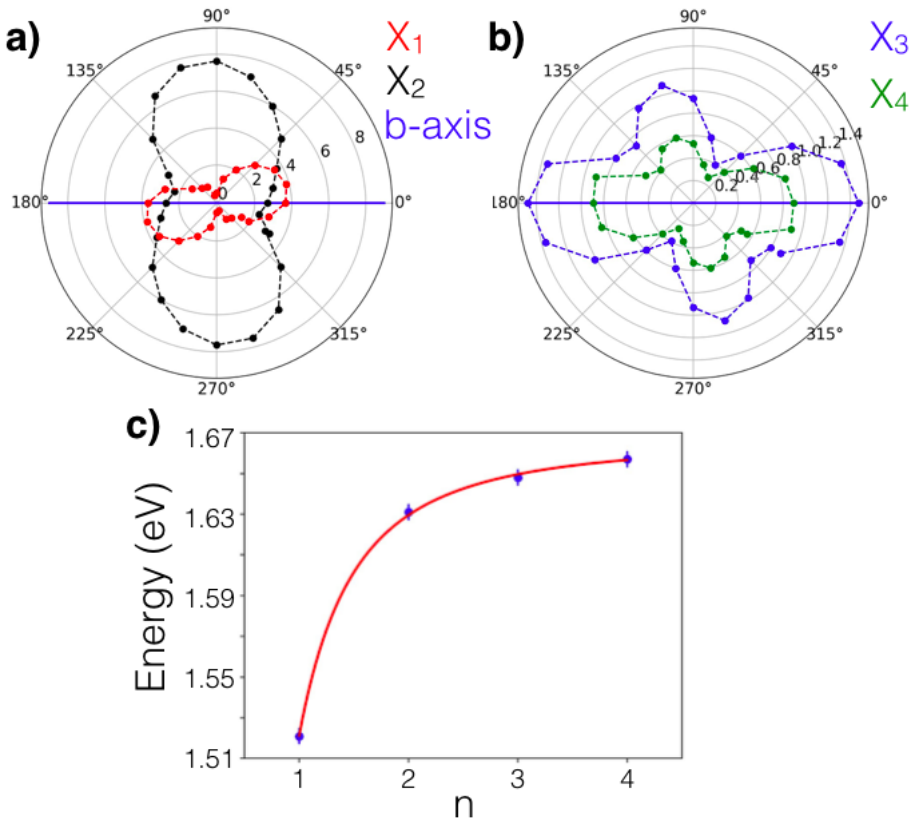

Figure 12: All data is taken from reflection measurements [44]. **a)** Polar plot for excitons X_1 and X_2. Both show a double lobed structure compared to a polarisation with respect to the b-axis. **b)** Polar plot for excitons X_3 and X_4. Both show a clover-like shape with maxima comparable with X_1 and X_2. **c)** Rydberg series of exciton X_1 with its suggested excited states fitted to Wannier excitons equation: $E_b^{(n)} = E_g - \frac{Ry^*}{n^2}$.

will make the peak narrower and perhaps show different peaks. Comparing the peak values to literature we expect X_3 to be a superposition of the first excited state of both polarisations (2s-orbital) and X_4 to be a superposition of all higher excited state of both polarisations [9]. This would explain the broad shoulder at the right of the X_4 peak, seen in Fig. 7c.

We also plotted the presumed ground state X_1 with its possible excited states and fit it to a Rydberg series given by equation 2, shown in Fig. 12c [9]. The fitted bandgap for exciton X_1 is $E_g = 1.665$ eV and a binding energy of 144 meV, which is in agreement with literature, corroborating the excited-state nature of peak X_3 [9]. There are not enough distinguishable peaks in the reflection measurements of excited states of X_2 to make a similar fit. Thus, lower temperature measurements are needed to know for certain if X_4 is a superposition of excited states.

Finally, we do the same power dependent PL measurement as for X_1 and X_2. The results are shown in Fig. 13a. Exciton X_3 is blue and exciton X_4 is green. The data points are fitted with the power function given by equation 5 and the β-parameter is shown for each fit. In the inset of Fig. 13a is a log-log plot shown where β is the slope and α is the offset. The fitted parameter values for X_3 are: $\alpha = 22(13)$ and $\beta = 1.09(28)$, and for X_4: $\alpha = 281(39)$

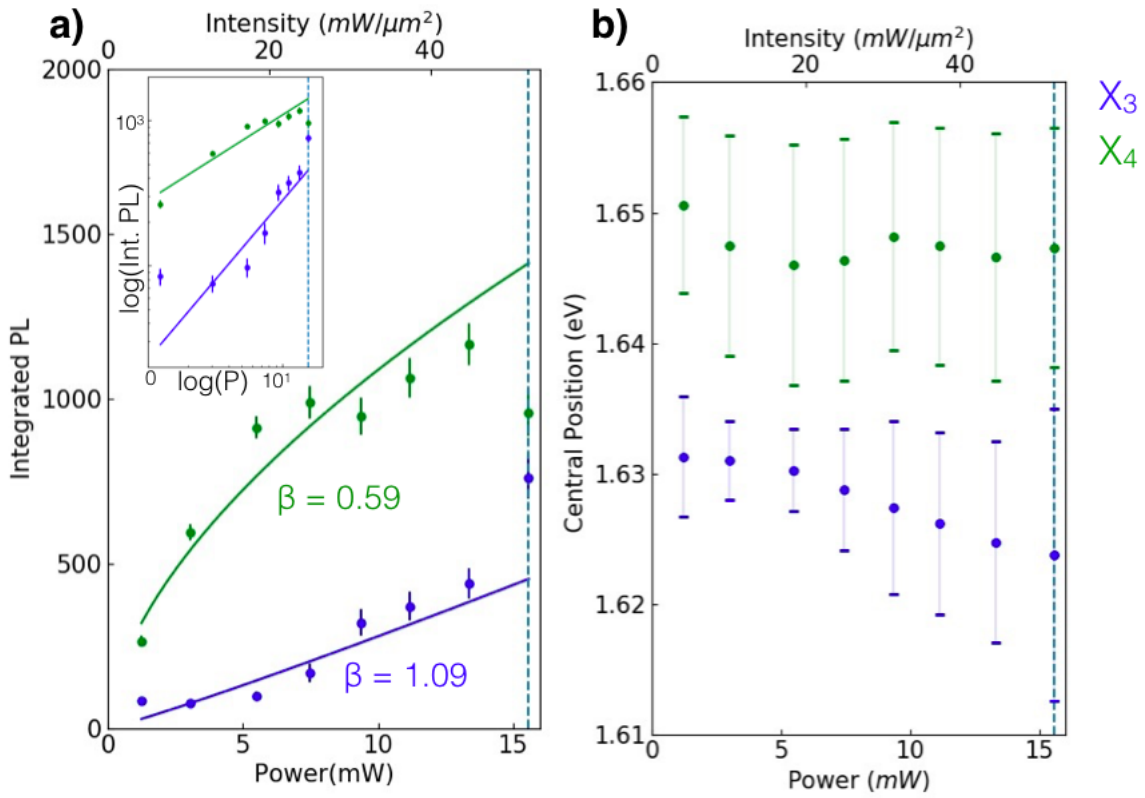

Figure 13: a) The integrated PL for exciton X_3 (blue) and exciton X_4 (green) as a function of laser power. The dashed blue line indicates when the sample got burned. Both dataset are fitted with the power function $I_{PL} = \alpha P^{\beta}$ and the β-parameter is shown for both excitons. **b)** The central position of exciton X_3 (blue) and exciton X_4 (green) as function of power. X_3 shows a small redshift for larger power but it unclear due to the large error while X_4 does not show a significant shift.

and $\beta = 0.59(7)$. Exciton X_4 shows a saturation curve quite similar to that of exciton X_2. Exciton X_3 has a high β-parameter, due to the large error it is not clear if it's bigger than 1.00, but it is not similar to the β-parameter of X_1. Fig. 13b shows the central position of the two exciton peak as a function of power. Exciton X_4 does not seem to have a significant shift at larger power. Exciton X_3 does show a redshift for higher power, also seen in Fig. 11. However, due to the high error on the central position this is still unclear. There is no trion peak observed in the PL spectrum, which would give an indication that the peak might be shifted due to a small bandgap renormalisation.

Since X_3 and X_4 are expected to be a superposition of multiple excited states is it difficult to argue what might (not) induce a saturation and redshift. To get a clearer view on this, lower temperature measurements might be a solution so the different peaks become distinguishable, and a more detailed analysis can be performed.

5 Discussion

In summary, we find two main linear polarised excitons peaks with a polarisation comparable to literature. From the PL spectra in Fig. 7c we see that X_2 has the highest amplitude, it is about 2 times bigger than the amplitude of X_1. However, if we compare it to the difference between indirect and direct bandgap amplitude for bulk MoS_2 which is a factor of 10 [7], it gives the indication that both exciton peaks are direct, which is consistent with recent experimental measurements [9]. However, the laser polarisation in the measurements is at 120° with respect to the b-axis, which is close to the maximum polarisation angle of X_2. This could mean that the laser gives a preference to the excitation of X_2 and that this is the reason why the amplitude of X_2 is bigger than X_1. To test if this is the case further measurements with a different laser polarisation needs to be done.

The laser power dependence measurements suggest a difference in lifetime. Literature has shown time-resolved PL measurements on 3L ReS_2 where they found lifetimes of <10 ps, which would indicate a direct bandgap [45]. However, they also preformed transient differential reflectance measurements where they observed 2 lifetime of <10 ps and ∼100 ps for both excitons, from which they conclude that both exciton transitions are a direct and indirect transitions close together in k-space even though 100 ps is still often attributed to a direct bandgap [45][46]. However, this was done on 3L whereas our measurements are done on bulk. In addition, a recent study measured a difference in the occurrence of saturation on two different monolayer TMDs while they both have a direct bandgap [29]. Thus, our measured difference in saturation, seen in Fig. 10a does not directly imply that a bandgap is direct or indirect but it indicates a difference in lifetime. Thus, lifetime measurements on bulk need to be done to get a more conclusive result.

The laser power dependence measurements also show a redshift at higher laser power for both exciton X_1 and X_2. This redshift might be due to a bandgap renormalisation or the presence of trions. Fig. 11 shows the PL spectra at different laser powers where the trion peaks T_1 and T_2 seems to "take over" the exciton peaks X_1 and X_2. A recent study modelled the recombination pathways in monolayer semiconductors [43]. It shows that both the radiative recombination and the non-radiative recombination grow with a higher generation rate, which indicated that the trion contribution in the PL spectra also grows at higher laser power. The probability of trion formation is fixed for a fixed background charge density. The higher the background charge density, the higher the probability of trion formation and thus a bigger contribution in the PL spectra. Unfortunately, we do not know the background charge density in our samples. Thus, the first step to figure out which processes play a roll, is to see if these peaks are indeed trions. Thereafter, investigate how these trion PL peaks change with a changing background charge density such as evaluated in a recent paper [43].

Furthermore, we find possible excited states of excitons X_1 and X_2. If we look back at Fig. 7b and follow the possible excited states peaks back to room temperature (303 K), the peak seem to follow from the right peak. This would mean that we can observe excited states at room temperature which is not expected for literature. For an (excited) exciton to exist at room temperature the binding energy needs to be larger than the thermal energy ($E_b > kT$). This means that binding energy of the excited state needs to be at least around 25 meV which is quite high for an excited state. To figure out the binding energy of the excited states a similar Rydberg series measurement could be done at lower temperature to get a more precise result. The calculated binding energies can then be compared to the thermal energy at room temperature to conclude if the excited states can stably exist at room temperature.

6 Conclusions and Outlook

In conclusion, we performed temperature and polarisation-resolved PL measurements to study the excitonic behaviour of bulk ReS_2. We find that there are two main exciton peaks observed in the PL spectra, which both show a linear polarisation with respect to the b-axis of $28(5)^\circ$ for exciton X_1 at an energy of 1.54(4) eV and an angle of $115(5)^\circ$ for exciton X_2 at an energy of 1.570(20) eV. Excitation power dependence measurements show that exciton X_1 saturates faster than exciton X_2. Both excitons are expected to be a direct transition, however they might have different lifetimes. It is still unclear what the process behind this is. It could be due to the difference in lifetime of the excitons or the involvement of trions which recombination process starts to dominate at higher power. Lifetime measurements and control over the charge density might shed a better light on this.

Possible excited states were also detected with reflection measurements, that match the peaks in PL, showing a good fit to the Rydberg series. The excited states show a polarisation similar to excitons X_1 and X_2, suggesting it to be a superposition of both polarisations. Power dependence measurements might suggest a small bandgap renormalisation at higher power but lower temperature measurements need to be done to unravel the different excited states and show a more conclusive result.

References

[1] Flagship report. Global energy review 2020. `https://www.iea.org/reports/global-energy-review-2020/renewables`, 4 (2020). *Accessed on 26-06-2020.*

[2] Nilofar Asim, Kamaruzzaman Sopian, Shideh Ahmadi, Kasra Saeedfar, MA Alghoul, Omidreza Saadatian, and Saleem H Zaidi. A review on the role of materials science in solar cells. *Renewable and Sustainable Energy Reviews*, **16** (8), p.5834-5847 (2012).

[3] Deep Jariwala, Artur R Davoyan, Joeson Wong, and Harry A Atwater. Van der Waals materials for atomically-thin photovoltaics: Promise and outlook. *ACS Photonics*, **12** (4), p. 2962-2970 (2017).

[4] Ah-Jin Cho, Kyung Park, Solah Park, Min-Kyu Song, Kwun-Bum Chung, and Jang-Yeon Kwon. A transparent solar cell based on a mechanically exfoliated GaTe and InGaZnO p–n heterojunction. *Journal of Materials Chemistry C*, **5** (17), p. 4327-4334 (2017).

[5] Mohammad Rahman, Kenneth Davey, and Shi-Zhang Qiao. Advent of 2D rhenium disulfide (ReS_2): Fundamentals to applications. *Advanced Functional Materials*, **27** (10), p. 1606129 (2017).

[6] Andrea Splendiani, Liang Sun, Yuanbo Zhang, Tianshu Li, Jonghwan Kim, Chi-Yung Chim, Giulia Galli, and Feng Wang. Emerging photoluminescence in monolayer MoS_2. *Nano letters (ACS Publications)*, **10** (4), p. 1271-1275 (2010.

[7] Kin Fai Mak, Changgu Lee, James Hone, Jie Shan, and Tony F Heinz. Atomically thin MoS_2: a new direct-gap semiconductor. *Physical review letters*, **105** (13), p. 136805 (2010).

[8] Mathias Gehlmann, Irene Aguilera, Gustav Bihlmayer, Slavomír Nemsak, Philipp Nagler, Pika Gospodaric, Giovanni Zamborlini, Markus Eschbach, Vitaliy Feyer, Florian Kronast, et al. Direct observation of the band gap transition in atomically thin ReS_2. *Nano letters*, **17** (9), p. 5187-5192 (2017).

[9] J Jadczak, J Kutrowska-Girzycka, T Smoleński, P Kossacki, YS Huang, and L Bryja. Exciton binding energy and hydrogenic rydberg series in layered ReS_2. *Scientific reports*, **9** (1) p.1-9 (2019).

[10] Daniel A Chenet, O Burak Aslan, Pinshane Y Huang, Chris Fan, Arend M van der Zande, Tony F Heinz, and James C Hone. In-plane anisotropy in mono- and few-layer ReS_2 probed by raman spectroscopy and scanning transmission electron microscopy. *Nano letters*, **15** (9), p.5667-5672 (2015).

[11] KS Novoselov and AH Castro Neto. Two-dimensional crystals-based heterostructures: materials with tailored properties. *Physica Scripta*, **2012** (146), p. 014006 (2012).

[12] Haifeng Wang, Erfu Liu, Yu Wang, Bo Wan, Ching-Hwa Ho, F Miao, and XG Wan. Cleavage tendency of anisotropic two-dimensional materials: ReX_2 (X= S, Se) and WTe_2. *Physical Review B*, **96** (16), p. 165418 (2017).

[13] Donald F Swinehart. The Beer-Lambert law. *Journal of chemical education*, **39** (7), p. 333 (1962).

[14] Qing Hua Wang, Kourosh Kalantar-Zadeh, Andras Kis, Jonathan N Coleman, and Michael S Strano. Electronics and optoelectronics of two-dimensional transition metal dichalcogenides. *Nature nanotechnology*, **7** (11), p. 699- 712 (2012).

[15] Yuhei Miyauchi. Photoluminescence studies on exciton photophysics in carbon nanotubes. *Journal of Materials Chemistry C*, **1** (40), p. 6499-6521 (2013).

[16] John R Hook and Henry Edgar Hall. *Solid state physics*. John Wiley & Sons, 1991.

[17] KP O'donnell and X Chen. Temperature dependence of semiconductor band gaps. *Applied physics letters*, **58** (25), p. 2924-2926 (1991).

[18] Yatendra Pal Varshni. Temperature dependence of the energy gap in semiconductors. *Physica*, **34** (1), p. 149-154 (1967).

[19] Biljana Pejova, Bahattin Abay, and Irina Bineva. Temperature dependence of the band-gap energy and sub-band-gap absorption tails in strongly quantized ZnSe nanocrystals deposited as thin films. *The Journal of Physical Chemistry C*, **114** (36), p. 15280-15291 (2010).

[20] Daniel V Schroeder. An introduction to thermal physics, 1999.

[21] Alexey Chernikov, Timothy C Berkelbach, Heather M Hill, Albert Rigosi, Yilei Li, Ozgur Burak Aslan, David R Reichman, Mark S Hybertsen, and Tony F Heinz. Exciton binding energy and nonhydrogenic rydberg series in monolayer WS_2. *Physical review letters*, **113** (7), p. 076802 (2014).

[22] Jun Mao, Zihang Liu, and Zhifeng Ren. Size effect in thermoelectric materials. *npj Quantum Materials*, **1** (1), p. 1-9 (2016).

[23] Miguel M Ugeda, Aaron J Bradley, Su-Fei Shi, H Felipe, Yi Zhang, Diana Y Qiu, Wei Ruan, Sung-Kwan Mo, Zahid Hussain, Zhi-Xun Shen, et al. Giant bandgap renormalization and excitonic effects in a monolayer transition metal dichalcogenide semiconductor. *Nature materials*, **13** 12, p. 1091-1095 (2014).

[24] Jiaqi He, Dawei He, Yongsheng Wang, Qiannan Cui, Frank Ceballos, and Hui Zhao. Spatiotemporal dynamics of excitons in monolayer and bulk WS_2. *Nanoscale*, **7** 21, p. 9526-9531 (2015).

[25] Claus F Klingshirn. *Semiconductor optics*. Springer Science & Business Media, 2012.

[26] Leslie Allen and Joseph H Eberly. *Optical resonance and two-level atoms. Courier Corporation*, **28** (1987).

[27] Philipp Tonndorf, Robert Schmidt, Robert Schneider, Johannes Kern, Michele Buscema, Gary A Steele, Andres Castellanos-Gomez, Herre SJ van der Zant, Steffen Michaelis de Vasconcellos, and Rudolf Bratschitsch. Single-photon emission from localized excitons in an atomically thin semiconductor. *Optica*, **2** (4), p. 347-352 (2015).

[28] M Manca, MM Glazov, Cédric Robert, F Cadiz, T Taniguchi, K Watanabe, E Courtade, Thierry Amand, Pierre Renucci, Xavier Marie, et al. Enabling valley selective exciton scattering in monolayer WSe_2 through upconversion. *Nature communications*, **8** (1), p. 1-7 (2017).

[29] Min Ju Shin, Dong Hak Kim, and Daeyoung Lim. Photoluminescence saturation and exciton decay dynamics in transition metal dichalcogenide monolayers. *Journal of the Korean Physical Society*, **65** (12), p. 2077-2081 (2014).

[30] Ozgur Burak Aslan, Daniel A Chenet, Arend M Van Der Zande, James C Hone, and Tony F Heinz. Linearly polarized excitons in single-and few-layer ReS_2 crystals. *ACS Photonics*, **3** (1), p. 96-101 (2016).

[31] Valentina Palanza, Daniela Di Martino, Alberto Paleari, Giorgio Spinolo, and Loredana Prosperi. Micro-raman spectroscopy applied to the study of inclusions within sapphire. *Journal of Raman Spectroscopy: An International Journal for Original Work in all Aspects of Raman Spectroscopy, Including Higher Order Processes, and also Brillouin and Rayleigh Scattering*, **39** (8), p. 1007-1011 (2008).

[32] Philipp Nagler, Gerd Plechinger, Christian Schüller, and Tobias Korn. Observation of anisotropic interlayer raman modes in few-layer ReS_2. *physica status solidi (RRL)–Rapid Research Letters*, **10** (2), p. 185-189 (2016).

[33] Hyejin Jang, Christopher R Ryder, Joshua D Wood, Mark C Hersam, and David G Cahill. 3D anisotropic thermal conductivity of exfoliated rhenium disulfide. *Advanced Materials*, **29** (35), p. 1700650 (2017).

[34] Yanqing Feng, Wei Zhou, Yaojia Wang, Jian Zhou, Erfu Liu, Yajun Fu, Zhenhua Ni, Xinglong Wu, Hongtao Yuan, Feng Miao, et al. Raman vibrational spectra of bulk to monolayer ReS_2 with lower symmetry. *Physical Review B*, **92** (5), p. 54-110 (2015).

[35] W Gough. The graphical analysis of a Lorentzian function and a differentiated Lorentzian function. *Journal of Physics A: General Physics*, **1** (6), p.704 (1968).

[36] John Taylor. *Introduction to error analysis, the study of uncertainties in physical measurements*. 1997.

[37] Lukas Novotny and Bert Hecht. *Principles of nano-optics*. Cambridge university press, 2012.

[38] Online protractor. `https://www.ginifab.com/feeds/angle_measurement/`. Accessed on 11-06-2020.

[39] Ching-Hwa Ho and Zhan-Zhi Liu. Complete-series excitonic dipole emissions in few layer ReS_2 and $ReSe_2$ observed by polarized photoluminescence spectroscopy. *Nano energy*, **56**, p. 641-650 (2019).

[40] Xiaofan Wang, Keisuke Shinokita, Yuhei Miyauchi, Nguyen Thanh Cuong, Susumu Okada, and Kazunari Matsuda. Experimental evidence of anisotropic and stable charged excitons (trions) in atomically thin 2D ReS_2. *Advanced Functional Materials*, **29** (51), p. 1905961 (2019).

[41] Matthew Z Bellus, Frank Ceballos, Hsin-Ying Chiu, and Hui Zhao. Tightly bound trions in transition metal dichalcogenide heterostructures. *ACS nano*, **9** (6), p. 6459-6464 (2015).

[42] Ashish Arora, Thorsten Deilmann, Till Reichenauer, Johannes Kern, Steffen Michaelis de Vasconcellos, Michael Rohlfing, and Rudolf Bratschitsch. Excited-state trions in monolayer WS_2. *Physical Review Letters*, **123** (16), p. 167401 (2019).

[43] Der-Hsien Lien, Shiekh Zia Uddin, Matthew Yeh, Matin Amani, Hyungjin Kim, Joel W Ager, Eli Yablonovitch, and Ali Javey. Electrical suppression of all nonradiative recombination pathways in monolayer semiconductors. *Science*, **364** (6439), p. 468-471 (2019).

[44] Floris Kienhuis. Probing anisotropic excitons in mechanically exfoliated rhenium disulfide through low temperature reflectance contrast spectroscopy. University of Amsterdam, July (2020). Bachelor's Thesis.

[45] Xiaofan Wang, Keisuke Shinokita, Hong En Lim, Nur Baizura Mohamed, Yuhei Miyauchi, Nguyen Thanh Cuong, Susumu Okada, and Kazunari Matsuda. Direct and indirect exciton dynamics in few-layered ReS_2 revealed by photoluminescence and pump-probe spectroscopy. *Advanced Functional Materials*, **29** (6), p. 1806169 (2019).

[46] Maurizia Palummo, Marco Bernardi, and Jeffrey C Grossman. Exciton radiative lifetimes in two-dimensional transition metal dichalcogenides. *Nano letters*, **15** (5), p. 2794-2800 (2015).